npj | 2D Materials and Applications

www.nature.com/npj2dmaterials

ARTICLE OPEN

Check for updates

Dominant role of two-photon vertex in nonlinear response in two-dimensional Dirac systems

Habib Rostami[1]✉ and Emmanuele Cappelluti[2]

We show that the standard concepts of nonlinear response to electromagnetic fields break down in two-dimensional Dirac systems, like graphene, in the quantum regime close to the Dirac point. We present a compelling many-body theory for nonlinear transport focusing on disorder scattering as a benchmark example. We show that, although the diamagnetic two-photon vertex is absent at the non-interacting level, disorder effects give rise to a self-generation of such two-photon vertex surviving even in the clean limit. We predict that the two-photon vertex self-generation is present only in two dimensions. The impact of such a striking scenario on the nonlinear quantum transport is discussed, predicting a huge enhancement of third-order dc conductivity comparing to the common models.

npj 2D Materials and Applications (2021)5:50 ; https://doi.org/10.1038/s41699-021-00217-0

INTRODUCTION

Due to their linear dispersion and the underlying chiral structure, Dirac materials (DMs) show a variety of exotic features that makes them a versatile platform for new physics and application purposes. Despite the complex physics, many properties of these materials are often rationalized using non-interacting or semi-classical models[1–4]. For instance, standard transport models are conventionally applied for the dc transport in highly doped DMs (*Boltzmann* regime), where the mobility is evaluated at the non-interacting level, and the interactions enter only through the effective transport scattering rate Γ_{tr}[5]. At odds with such scenario, there is a wide consensus that the *quantum* regime (low-energy transitions in undoped Dirac model) is much more complex and significantly affected by many-body effects[6].

The nonlinear response of DMs has attracted recently a considerable interest in two[7–14] and three dimensions[15–21]. Widely investigated are the nonlinear optical properties such as four-wave mixing, nonlinear Kerr effect, high-harmonic-generations in single-layer graphene, with remarkable technological interests[22–32]. Peculiar of DM is, due to the linear dispersion, the absence of bare two-photon-electron coupling, which should rule the so-called *diamagnetic* term[33]. The lack of such a term prompts several widely debated issues, as the validity of optical sum rules[34–36]. Most of the theoretical descriptions of nonlinear effects rely currently upon non-interacting or semiclassical approaches[24–26,37–44] where, similar to the linear Boltzmann theory, the relaxation processes are accounted through effective scattering rates Γ (equivalently mean-free-paths, ℓ, or lifetimes, τ).

In this work, we show that a compelling analysis of many-body physics, beyond the semiclassical approaches, can drastically change the above scenario, pointing out that different physical processes can be responsible for the relevant properties of the nonlinear dc transport. Analyzing disorder scattering case as a benchmark example, we show how non-conserving phenomenological models of scattering intrinsically fail and high-order vertex processes must be properly taken into account. Moreover, in particular, we show that despite the bare diamagnetic two-photon vertex (TPV) being null in DMs, the many-body renormalized TPV is finite and it plays a dominant role. Our results, besides providing a consistent framework for a proper analysis of nonlinear transport and optics in interacting DMs, open different perspectives for understanding and predicting new functional properties of these promising systems.

RESULTS

Two-dimensional DMs model

We consider two-dimensional (2D) Dirac Hamiltonian $\hat{\mathcal{H}}_{\mathbf{k}} = \hbar v \hat{\boldsymbol{\sigma}} \cdot \mathbf{k} - \mu_0 \hat{I}$, where μ_0 is the bare chemical potential. For realistic purposes, we consider the paradigmatic case of graphene, $\hat{\boldsymbol{\sigma}} = (\tau\hat{\sigma}_x, \hat{\sigma}_y)$, where $\hat{\sigma}_i$ stands for the Pauli matrices in the spinor space, and $\tau = \pm$ stands for the time-reversal counterparts, valley index. Light–matter interaction in the dipole approximation is modeled by applying the minimal coupling transformation $\hbar\mathbf{k} \to \hbar\mathbf{k} + e\mathbf{A}(t)$ with $\mathbf{A}(t)$ as an external vector potential. The corresponding electric field follows $\mathbf{E}(t) = -\partial_t \mathbf{A}(t)$. Due to the linear dispersion, the electron-photon coupling presents no diamagnetic (two-photon) bare term but only the linear coupling:

$$\mathcal{H}_{\text{light-matter}} = \hbar e v \int d\mathbf{r}\, \hat{\psi}^{\dagger}(\mathbf{r}) \hat{\boldsymbol{\sigma}} \cdot \mathbf{A}(t) \hat{\psi}(\mathbf{r})\,. \tag{1}$$

Without loss of generality, we assume an electric field along y. As a scattering source, we consider long-range impurities within the context of the self-consistent Born approximation[45–47]. Such a scattering model, although not exhaustive[5,48] and neglecting relevant sources of interaction as the electron–electron coupling[49–52], is particular useful since it represents the simplest context pointing out how a conserving approach is needed and how multi-photon vertices play a crucial role in nonlinear transport. In this context, we focus on the intra-valley long-range impurity scattering in this study since for the inter-valley short-range Born impurity scattering it was shown that the vertex correction average to zero[45,46].

Within this framework we write the impurity self-energy in the absence of external field in the complex frequency space: $\hat{\Sigma}(z) = \gamma_{\text{imp}} \sum_{\mathbf{k}} \hat{G}(\mathbf{k}, z)$ where the Green's function follows

[1]Nordita, KTH Royal Institute of Technology and Stockholm University, Hannes Alfvéns väg 12, 10691 Stockholm, Sweden. [2]Istituto di Struttura della Materia-CNR (ISM-CNR), Trieste, Italy. ✉email: habib.rostami@su.se

$\hat{G}(\mathbf{k},z)=[z-\hat{\mathcal{H}}_{\mathbf{k}}-\hat{\Sigma}(z)]^{-1}$. For isotropic scattering we get a diagonal self-energy in the spinor basis: $\hat{\Sigma}(z)=\Sigma(z)\hat{I}$. Under these conditions, the impurity self-energy, as well as the Coulomb and other scattering ones, depends intrinsically on the ultraviolet energy cut-off W representing the range of validity of the Dirac model. To provide a conserving approach, as detailed in Supplementary Note 1, we employ standard dimensional regularization[53,54] leading to:

$$\Sigma(z)=-US(z)\ln\left[-W^2/S(z)^2\right], \tag{2}$$

where $S(z)=z+\mu_0-\Sigma(z)$, and U is a dimensionless parameter characterizing scattering strength (see Eq. (7) of Supplementary Information).

Interacting nonlinear response theory

Conserving approaches, based for instance on a Baym–Kadanoff derivation[55,56], are fundamental in theoretical physics to enforce the validity of the conservation laws (i.e., the continuity equation) and to ensure compelling results. This aim is particularly important in nonlinear response since an arbitrary selection of diagrams can easily lead to spurious conclusions. The choice of the vector-potential gauge, within the paradigmatic Born impurity scattering here consider, permits an exact derivation of self-consistent equations (see Supplementary Note 2) for all high-order processes relevant in the third-order response function which is the leading nonlinear term in centrosymmetric DMs. The diagrammatic expression of the third-order response is provided in Fig. 1a where empty symbols represent the unrenormalized n-photon vertices, whereas filled symbols represent the solution of a Bethe–Salpeter (BS) self-consistent resummation for a given n-photon vertex (Fig. 1b–d). The bare multi-photon vertices are expressed in terms of the renormalized lower-order vertices (Fig. 1e, f). The TPV function is defined in terms second derivative of field-dependent Green's function inverse $\hat{G}^{-1}=\hat{G}_0^{-1}-\hat{\Sigma}_A$:

$$\hat{\Lambda}_2(1,2)=\frac{\delta^2\hat{G}^{-1}}{\delta A(1)\delta A(2)}\Big|_{A\to 0}, \tag{3}$$

where $\hat{\Sigma}_A(1,2)=\hat{\Sigma}(1,2;\mathbf{A})$ is the self-energy in the presence of the external field $\mathbf{A}$ (see Supplementary Note 2). Note that 1 stands for space-time coordinate ($\mathbf{r}_1$, t_1) and external vector potential is assumed to be along a particular direction with magnitude $A(1)$. The second derivative of the bare Green's function $\hat{G}_0$ vanishes in Dirac systems which implies the absence of bare TPV. However, an interaction-induced TPV function is obtained owing to the field-dependent self-energy. In the Born approximation, the self-energy is linear in the Green's function $\hat{\Sigma}=V\hat{G}$ with V being the inter-particle interaction potential. Since the self-energy depends on the external field only through the dependence on the Green's function, we have

$$\hat{\Lambda}_2(1,2)=-V\frac{\delta^2\hat{G}}{\delta A(1)\delta A(2)}\Big|_{A\to 0}. \tag{4}$$

It is straightforward to evaluate the second derivative of the Green's function and obtain the following relation in terms of the zero-field Green's function (see Supplementary Note 2)

$$\hat{\Lambda}_2(1,2)=\hat{\Lambda}_2^{(0)}(1,2)+V\hat{G}\hat{\Lambda}_2(1,2)\hat{G}, \tag{5}$$

where the interaction-induced bare two-photon vertex coupling reads

$$\hat{\Lambda}_2^{(0)}(1,2)=-\sum_{\mathcal{P}(1;2)}V\hat{G}\hat{\Lambda}_1(1)\hat{G}\hat{\Lambda}_1(2)\hat{G}. \tag{6}$$

Note that $\hat{\Lambda}_1(1)=\delta\hat{G}/\delta A(1)|_{A\to 0}$ stands for the renormalized one-photon vertex coupling and $\mathcal{P}(1;2)$ indicates the permutation between 1 and 2 labels. The self-consistent BS relation given in Eq. (5) and bare TPV Eq. (6) are diagrammatically illustrated in Fig. 1c and Fig. 1e, respectively. Using a similar functional derivative technique one can algebraically prove all diagrammatic relations represented in Fig. 1.

Few relevant things are worth to be underlined here. First of all, we notice that an effective multi-photon coupling is induced by the disorder scattering even if absent in the bare Hamiltonian (Fig. 1e, f). Second, that the relevance of each n-photon vertex is largely governed by the BS resummation as depicted in Fig. 1b–d.

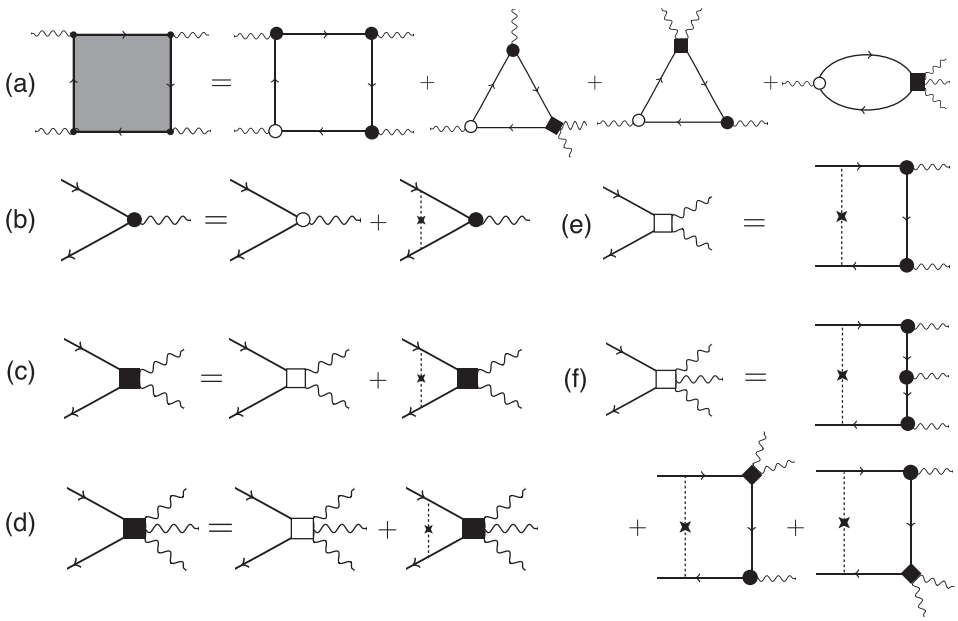

Fig. 1 Diagrammatic representation of nonlinear e.m. response in Dirac materials. a nonlinear response expressed in terms of *renormalized* n-photon vertices; **b**–**d** self-consistent Bethe–Salpeter equations for one-, two- and three-photon vertices; **e**–**f** many-body definition of *unrenormalized* two- and three-photon vertices in terms of lower-order vertices. Solid and wavy lines stand for fermion propagator and external photons, respectively. Dashed lines indicate impurity interaction. Empty/filled circles stand for bare/renormalized one-photon vertex, respectively. Empty/filled squares stand for unrenormalized/renormalized two and three-photon vertices.

This might lead to a reduction (screening) or enhancement of different multi-photon scattering depending on the Pauli structure of the corresponding vertex, as discussed extensively later. We highlight that the Green's function method based on the Baym–Kadanoff framework[55] is constructed in such a way that it automatically satisfies particle conservation law (known as the continuity relation) as well as the momentum, energy and angular momentum conservations are fulfilled.

Universal scaling of nonlinear conductivity

The diagrammatic expressions in Fig. 1 represent in full generality the third-order response function in DMs, including third-harmonic generation, four-wave mixing, etc. For generic interaction, the solution of such coupled equations on the real-frequency axis is a formidable task. The focus on isotropic disorder scattering is particularly suitable to investigate many-body effects in the nonlinear response since it allows for a set of equations in Matsubara space which can be generalized in a rigorous way on the real axis, using the standard procedure of multiple branch cuts in the complex frequency space. The derivation (lengthly and cumbersome but compelling) is summarized in Supplementary Notes 3 and 4. We consider first the dc transport limit. Without loss of generality, we can express the linear and third-order dc conductivities in terms of dimensionless quantities:

$$\sigma_{\rm dc}^{(1)} = \sigma_0 f_1\left(\frac{\mu}{\Gamma(\mu)};U\right), \tag{7}$$

$$\sigma_{\rm dc}^{(3)} = \frac{\sigma_0}{E_0^2}\left[\frac{t_0}{\Gamma(\mu)}\right]^4 f_3\left(\frac{\mu}{\Gamma(\mu)};U\right), \tag{8}$$

where $\mu = \mu_0 - {\rm Re}\Sigma(\omega=0)$ is the effective chemical potential, $\Gamma(\mu) = -{\rm Im}\Sigma(\omega=0)$ is the scattering rate, $\sigma_0 \propto e^2/\hbar$ is the universal conductivity and $E_0 \propto t_0/ea$ is a characteristic electric-field scale determined by the inter-atomic hopping energy t_0 and by the lattice constant a.

We stress again that Eqs. (7) and (8) are tied together since they must descend in a compelling way from a common self-energy approximation. Heretofore, although many self-energy paradigms have been discussed for the linear response, the third-order response has been analyzed only in the simplistic case of a phenomenological constant scattering rate $\Sigma = -i\Gamma$. Since such phenomenological self-energy does not depend on the external field, the third-order response function reduces to the first "square" diagram of Fig. 1a dropping all the vertex renormalization processes, i.e., replacing the filled circles with empty ones. A similar scheme can be employed for the linear response. Under these ultra-simplified conditions, the linear and third-order dc transport depend uniquely on the semiclassical parameter $x = \mu/\Gamma$, i.e., $f_1(x;y) = f_1(x)$, $f_3(x;y) = f_3(x)$. The analytical expressions for the functions $f_1(x)$ and $f_3(x)$ are obtained in Supplementary Notes 5 and 6A, respectively. In particular, in the Boltzmann regime, one gets $f_1(\infty) \approx 2\mu/\pi\Gamma$, $f_3(\infty) \approx -3\pi\Gamma/32\mu$, implying a nonlinear *reduction* of the dc conductivity. A similar analysis is performed in the quantum regime, giving $f_1(0) = 8/\pi^2$, $f_3(0) = 2/5$, implying an *enhancement* of the dc conductivity in the quantum regime due to nonlinear effects.

The above predictions, based on the phenomenological constant-Γ model, are challenged when many-body effects are computed in a compelling conserving scheme. We estimate the third-order dc conductivity as $\sigma_{\rm dc}^{(3)} = \lim_{\omega\to 0}\sigma_{\rm THG}^{(3)}(\omega)$ where $\sigma_{\rm THG}^{(3)}(\omega)$ is the third-harmonic generation conductivity (see Supplementary Note 6B for details). In Fig. 2a, b we show the characteristic dc transport function f_3 as a function of the parameter $x = \mu/\Gamma(\mu)$, from the extreme quantum limit ($x \ll 1$) to the Boltzmann regime ($x \gg 1$). From the computational point of view, since the presence of a finite cut-off energy W, the quantum limit is conveniently investigated by fixing U and varying μ, whereas the Boltzmann regime is more easily spanned fixing μ and varying U. We discuss first the Boltzmann regime (Fig. 2b). We notice that a full many-body analysis recovers qualitatively the predictions of the constant-Γ model with $f_3(x,y) \approx f_3(x) \propto -1/x$ in the Boltzmann regime $x \gg x^* \approx 10$. The quantitative mismatch in the Boltzmann limit between our full quantum theory and constant-Γ model (as well as the phenomenological density matrix approach[24–26,29]) can be ascribed to a good extend to the lack, in the phenomenological constant-Γ models, of the all vertex renormalization processes which are known already at the linear transport level to give rise in a quantum treatment for isotropic impurity scattering to an additional factor $\Gamma_{\rm tr} = \Gamma\langle(1-\cos\theta)(1+\cos\theta)\rangle = \Gamma/2$ (see refs. [45,46,57] and also Supplementary Note 5). This leads roughly to a mismatch factor $16 = 2^3 \times 2$ between constant-Γ model and the full quantum theory where 2^3 comes from the three one-photon renormalization factors corresponding to black vertex dots in the square diagram in Fig. 1a and an extra 2 is the net effect of three-photon bubble diagram contribution (see the last diagram in Fig. 1a).

On the other hand, in the quantum regime $x \ll x^*$ (Fig. 2a), f_3 shows a significant dependence on μ_0, signalizing that the

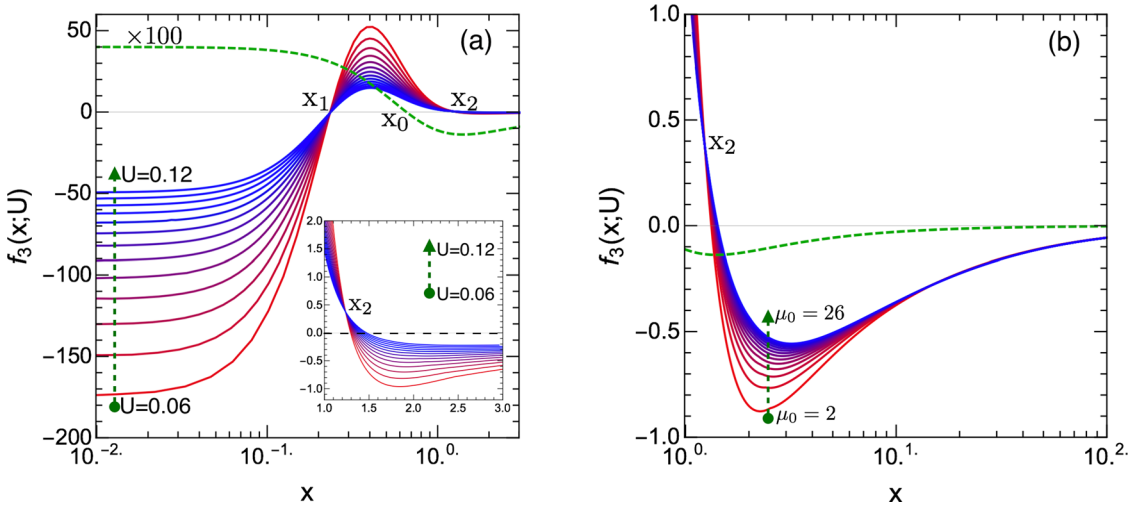

Fig. 2 Nonlinear dc conductivity in 2D Dirac materials. Characteristic nonlinear transport function f_3 versus the dimensionless parameter $x = \mu/\Gamma(\mu)$ within the many-body conserving scheme. Also shown is f_3 for the phenomenological model (dashed green line). Curves of f_3 versus x are plotted for different U's in the quantum regime (**a**), and for different μ_0's in the Boltzmann regime in THz unit (**b**).

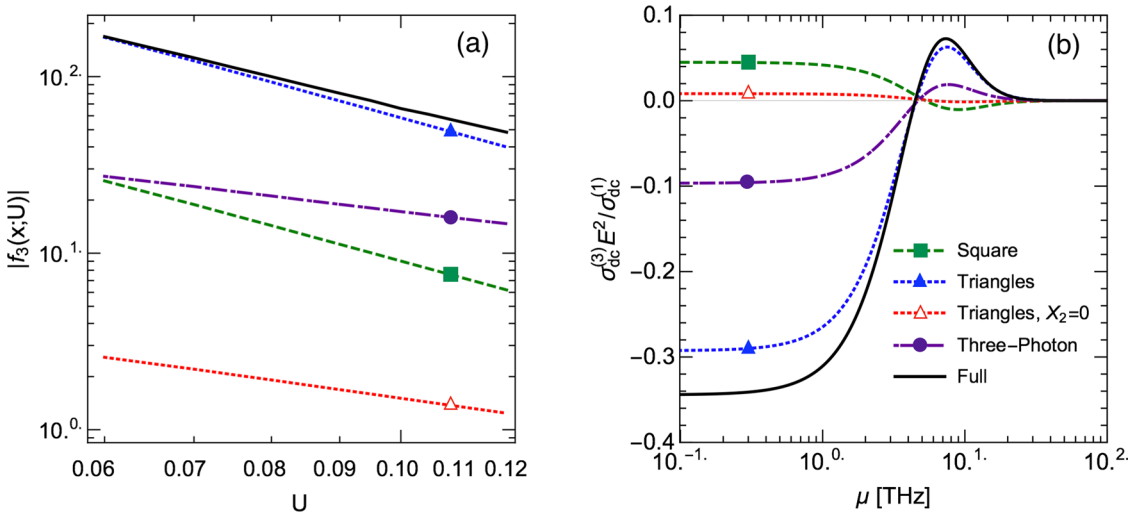

Fig. 3 Universal scaling of nonlinear dc conductivity in 2D Dirac materials. a Log–log scale plot for the absolute value of the characteristic third-order transport function $f_3(\mu, U)$ versus U at $x = 0.03$. Different lines correspond to the individual contribution of diagrams in Fig. 1a as mentioned the shared plot-legend in (**b**). **b** Nonlinear correction $g = |\sigma^{(3)}_{dc}|E^2/\sigma^{(1)}_{dc}$ at external electric-field $E = 1$ mV/nm is shown versus the chemical potential μ for $U = 0.11$. Similar to (**a**), different curves correspond to different diagram's contribution as mentioned the plot-legend.

nonlinear transport is no more governed uniquely by the semiclassical parameter x but the value of μ_0 (or conversely, U) starts playing a relevant role. Some striking things are worth being pointed out: (i) counterintuitively, the third-order contribution to the dc transport appears to be magnified approaching the clean limit $U \to 0$; (ii) there are two isosbestic points (i.e., x-points where f_3 does not depend on U) coinciding in a very good approximation with f_3-function zeroes; (iii) the phenomenological constant-Γ model predicts a well-determined positive sign of the nonlinear correction in the quantum regime (implying an increase of the total conductivity) whereas this sign in the quantum regime of the full conserving many-body theory is not univocally determined, presenting a positive crossover to negative sign in the extreme quantum limit.

We rationalize points (i)-(ii) by assuming that in the quantum regime the nonlinear characteristic transport function $f_3(x; U)$ can be factorized as:

$$f_3(x;U) \approx C(x)/U^{\gamma}, \tag{9}$$

(with $\gamma > 0$), where the strength of interaction U rules the *intensity* of the third-order transport, while the semiclassical parameter x dictates the *sign* of the correction. To assess the robustness of such a description we plot in Fig. 3a the absolute value of the function $f_3(x; U)$ versus U for a representative case $x = 0.03$ in the quantum regime. We find a perfect agreement with a scaling behavior $f_3(x; U) \propto 1/U^{\gamma}$ with γ slightly smaller than 2 ($\gamma = 1.82$) signalizing that in the clean limit the third-order transport is expected to dominate the linear one. As detailed in Supplementary Fig. 5, a similar analysis is valid in the whole quantum regime.

DISCUSSIONS

Two-photon vertex self-generation

To fully understand these interesting features, we analyze separately in Fig. 3a, b the relevance of each diagram contributing to the total third-order conductivity as depicted in Fig. 1a. We can realize that the contribution of the conventional "square" diagram (which is the only one present in the non-interacting case and for the constant-Γ model), is essentially marginal, as well as the contribution of the last "bubble" associated with the renormalized three-photon vertex. The dominant role is instead played by the "triangle" diagrams containing the renormalized TPV. A quantitative analysis shows that each family of diagrams obeys Eq. (9) with an approximately integer exponent (i.e., $\gamma_{\blacksquare} \approx 2$, $\gamma_{\blacktriangle} \approx 2$, and $\gamma_{\bullet} \approx 1$ for the square, triangle and the bubble diagrams). The dominance of the triangle diagrams results in an exponent very close to 2 ($\gamma \approx \gamma_{\blacktriangle}$). The self-consistent BS renormalization of the TPV (Fig. 1c) is a crucial ingredient in such a nontrivial scenario. This can be assessed in Fig. 3a, b where once neglected the BS renormalization, the contribution of the triangle diagrams is of the same order (even smaller) of that of the conventional square diagram. The dominant role of the TPV renormalization appears even more evident by investigating the scaling of the third-order transport function $f_3(x; U)$ versus U. As depicted in Fig. 3a, once replaced the BS renormalized TPV (Fig. 1c) with the "bare" one (Fig. 1e), the third-order dc conductivity scales as $1/U$ ($\gamma_{\triangle} \approx 1$), with an additional sign-change, as shown in Fig. 3b. This means that the BS renormalization of the TPV gives rise in the quantum regime to an additional dependence $\sim 1/U$ that diverges in the clean limit.

The n-photon vertex matrix structure, $\hat{\Lambda}_n = (-ev\hat{\sigma}_y)^n \Lambda_n$, plays a crucial role in the relevance of the BS renormalization effect. The impressive effect is peculiar of the TPV renormalization $\Lambda_2 = \Lambda_2^{(0)}/[1 - UX_2]$ and does not appear in the BS renormalization of the one- three-photon vertex ($\Lambda_n = \Lambda_n^{(0)}/[1 - UX_n]$, with $n = 1, 3$ and see Supplementary Notes 3B–D for details). This different impact can be traced down to the different Pauli structure in the spinor space. As detailed in Eq. (65) and Eq. (76) of Supplementary Information we get $X_1 = X_3 \propto \mathrm{Tr}[\hat{\sigma}_y \hat{G} \hat{\sigma}_y \hat{G}]$, $X_2 \propto \mathrm{Tr}[\hat{G}\hat{G}]$. In the quantum regime, one can thus show that in the dc limit $UX_1 \approx UX_3 \propto U$, whereas $UX_2 \approx 1 + \mathcal{O}(U)$, resulting in an effective divergence of $\Lambda_2/\Lambda_2^{(0)}$ at zero temperature and in the clean limit ($U \to 0$). The impact of the two-photon renormalization can be understood in more details by investigating the two-photon renormalization factor in an arbitrary spatial dimension (see Supplementary Note 3C for details),

$$Q_2(z_1, z_2) = \frac{1}{1 - UX_2(z_1, z_2)} = \frac{S(z_1) - S(z_2)}{z_1 - z_2}, \tag{10}$$

where $X_2(z_1, z_2) \propto \sum_{\mathbf{k}} \mathrm{Tr}[\hat{G}(\mathbf{k}, z_1)\hat{G}(\mathbf{k}, z_2)]$ and where z_1 and z_2 are the electronic frequencies in the complex plane. Particularly enlightening is the analysis of the retarded-retarded (RR) channel. In the dc limit ($\omega \to 0$) $Q_2^{\mathrm{RR}}(\epsilon, \epsilon + \hbar\omega)$ of 2D DMs is simply given by

(see Supplementary Note 7)

$$\lim_{\omega\to 0} Q_2^{\mathrm{RR}}(\epsilon,\epsilon+\hbar\omega)=\frac{dS(\epsilon)}{d\epsilon}=\frac{S(\epsilon)}{2US(\epsilon)+\mu_0+\epsilon}, \tag{11}$$

where $\hbar\omega$ is the photon energy and ϵ is the electronic energy. For low-energy excitations $\epsilon\approx 0$ we have $Q_2^{\mathrm{RR}}=S(0)/[2US(0)+\mu_0]$. The Boltzmann regime is achieved as $\mu_0\gg 2US(0)$. In the clean limit $U\to 0$ we get $S(0)=\mu_0$ and $Q_2^{\mathrm{RR}}=1$. The quantum regime is on the other hand characterized by $\mu_0\ll 2US(0)$, so that $Q_2^{\mathrm{RR}}=1/2U$, leading thus to a huge *enhancement* for $U\to 0$ as long as $\mu_0\ll 2US(0)$. A similar behavior $Q_2\propto 1/U$ appears also in the retarded-advance (RA) channel, although more delicately (see Supplementary Note 7 for details). As a net result, there is a divergence $1/\omega$ in $Q_2^{\mathrm{RA}}(\epsilon,\epsilon+\hbar\omega)$ at a low frequency which is reflected in a consequent divergence $-1/U$, similarly as for the RR channel, but with a *negative* sign. The balance between RR and RA terms determines the sign-change of the third-order dc conductivity versus x in the quantum regime. We must stress that the huge enhancement of the third-order dc transport is governed by the dominant role of the TPV renormalization. Since $\Lambda_2^{(0)}$ scales as U and $1/[1-UX_2]$ scales as $1/U$, such enhancement can be regarded as TPV self-generation ($\Lambda_2\neq 0$) which survives in the weak-coupling (clean) limit $U\to 0$.

Phase diagram and quantitative predictions in graphene

The net result on the dc transport is summarized in Fig. 4a where we plot the sign and the magnitude of the third-order conductivity for a representative electric field $E=1$ mV/nm[58–60] normalized to the linear order conductivity,

$$g(E)=\left|\sigma_{\mathrm{dc}}^{(3)}E^2/\sigma_{\mathrm{dc}}^{(1)}\right|, \tag{12}$$

in the physical space of the effective chemical potential μ and scattering rate $\Gamma(\mu)$, as they can be obtained directly in an experimental way. The Boltzmann regime corresponds thus to the right-lower corner whereas the extreme quantum regime ($x\to 0$) is recovered in the left-upper corner. As noticed before, at odds with the predictions of the phenomenological model, we find that the third-order conductivity $\sigma_{\mathrm{dc}}^{(3)}$ is negative not only in the Boltzmann regime but also in the *quantum* regime. Note that the zeroes of the third-order dc conductivity, see x_1 and x_2 in Fig. 2a, appear in this plot as straight dashed lines. This is a consequence of the factorizable expression for the characteristic third-order dc transport function as shown in Eq. (9). We mark with tiny dotted in this plot the regions where the third-order terms start to be relevant $g\approx 0.1$ and where they become of the same order than the linear dc term $g\approx 1$. Note that the condition $g=1$, in the regions where the third-order dc conductivity $\sigma_{\mathrm{dc}}^{(3)}$ is negative should not be regarded as an onset of *negative* total dc conductivity, rather as a sign that the expansion at the third-order in E starts to be a poor approximation and higher-order terms in powers of E must be included in the analysis. In Fig. 4b, we show the phase diagram for the constant-Γ model. As it is seen this phase diagram is completely different from that of the full quantum theory which is given panel (a). We can see only one sign-change in the constant-Γ model in contrast to that of full quantum theory which gives two sign-changes. Unlike the full quantum theory, the constant-Γ model predicts a positive nonlinear correction in the quantum regime.

We now assess the relevance of the nonlinear conductivity in graphene as a paradigmatic 2D DM. In particular, we consider a honeycomb lattice with inter-atom distance $b=1.42$ Å, with lattice parameter $a=\sqrt{3}b=2.46$ Å and nearest-neighbor hopping $t_0\approx 3$ eV, corresponding to a Dirac velocity $v=\sqrt{3}t_0a/2\hbar\approx 10^6$ m/s. Note that we have $\sigma_0=e^2/4\hbar$ and $E_0=\pi t_0/\sqrt{3}ea\approx 22.0\,\mathrm{V/nm}$ is an ultra-strong characteristic electric field. We define an ultraviolet energy cut-off $W=7.2$ eV for the Dirac linear dispersion (see Supplementary Note 1 for details). We evaluate the ratio $g(E)$ between the third-order and the linear order responses, as defined in Eq. (12). A critical electric-field E_{max} is defined as the electric-field above which third-order corrections become of the same order of the linear term, i.e., $g(E_{\mathrm{max}})=1$. The relevance of the third-order term compared with the linear contribution is investigated in an extended way shown in Fig. 4 in the generic μ-Γ phase diagram. In the phenomenological constant-Γ model we obtain $E_{\mathrm{max}}=\alpha E_0$ with $\alpha\approx 1.47\times\mu\Gamma/t_0^2$ in the Boltzmann regime and $\alpha\approx 1.42\times\Gamma^2/t_0^2$ in the quantum limit. These values can be compared with the estimates for the full conserving theory that gives $\alpha\approx 0.32\times\mu\Gamma(\mu)/t_0^2$ in the Boltzmann regime and $\alpha\approx 1.14U\times\Gamma(0)^2/t_0^2$ in the quantum limit with $U=1/\ln[W^2/\Gamma^2(0)]$. In Ref. [61] a roughly constant value $\Gamma\approx 15$ meV was estimated in the wide range $\mu\sim 0-200$ meV. With these values the phenomenological constant-Γ model would estimate a critical field $E_{\mathrm{max}}\approx 10.8$ mV/nm for $\mu\approx 200$ meV and $E_{\mathrm{max}}\approx 0.8$ mV/nm for $\mu=0$ with a quantum-Boltzmann crossover at $\mu^*\approx 150$ meV, whereas the full conserving theory predicts $E_{\mathrm{max}}\approx 2.35$ mV/nm for $\mu\approx 200$ meV and $E_{\mathrm{max}}\approx 0.05$ mV/nm for $\mu=0$, in a more observable range[58–60]. In realistic

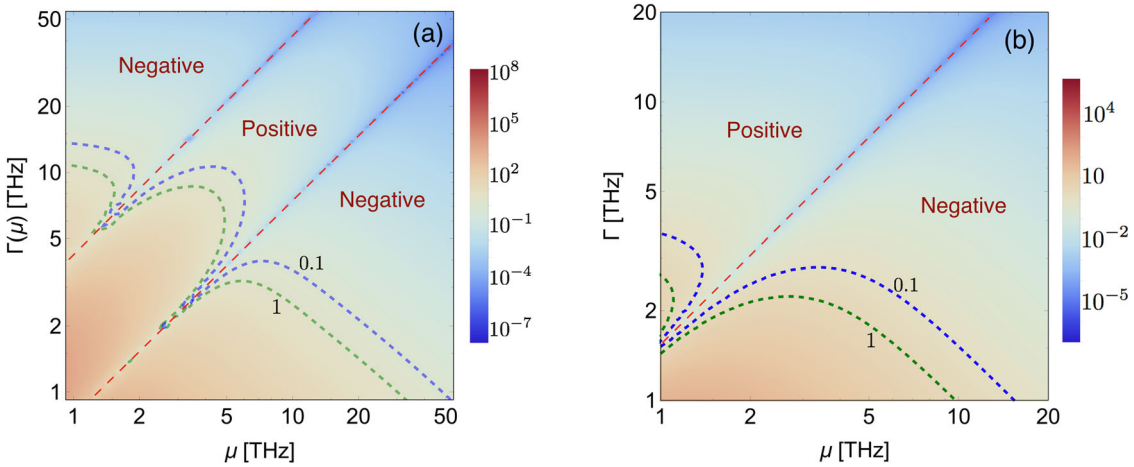

Fig. 4 Phase diagram for the nonlinear transport regimes in 2D Dirac materials. Colormap plot for $g=|\sigma_{\mathrm{dc}}^{(3)}E^2/\sigma_{\mathrm{dc}}^{(1)}|$ factor with $E=1$mV/nm versus chemical potential μ and relaxation rate $\Gamma(\mu)$ in the full conserving and constant-Γ models depicted in (**a**) and (**b**), respectively. The sign of $\sigma_{\mathrm{dc}}^{(3)}$ is written on the plot where two sign-switch borders are highlighted by dashed red lines. Green and blue dashed lines stand for the contour lines with $g=1$ and $g=0.1$, respectively.

experimental conditions, the electronic temperature raises due to high electric field, and thus a finite temperature analysis is needed to explain the experiments.

In summary, we have presented a fully conserving theory of nonlinear transport in DMs in the presence of disorder scattering. The predicted two-photon vertex self-generation is an intrinsic property of 2D systems which is absent in other dimensions (see Supplementary Note 7 for details). Our results show that the previous analyses in literature, based on phenomenological scattering models, can be qualitatively (but not quantitatively) reliable in the Boltzmann regime but they completely fail in the quantum regime. We have shown that, in a wide quantum region close to the neutral point, the nonlinear transport response is dominated by different physical processes where the TPV, absent in the non-interacting Dirac Hamiltonian, plays a relevant role. Our results, focused on the dc limit, imply that the current knowledge about the nonlinear optical response in the terahertz regime should be deeply revised as well. The TPV self-generation is particularly important in difference-frequency nonlinear phenomena such as photogalvanic effect, two-photon absorption, and stimulated Raman effect where there is always a low (infrared or even dc) frequency component for which the self-generation condition is satisfied. Our work, which paves the way for a further generalization to include in a conserving way the electron–phonon and electron–electron scattering channels for going beyond standard hydrodynamic and mean-field density matrix analysis, opens new perspectives to deeply understand the nonlinear response of Dirac systems, whose relevance ranges from condensed matter to high-energy physics.

DATA AVAILABILITY

All data that support the findings of this study are available on request from the corresponding author.

Received: 24 August 2020; Accepted: 9 March 2021;
Published online: 13 May 2021

REFERENCES

1. Castro Neto, A. H., Guinea, F., Peres, N. M. R., Novoselov, K. S. & Geim, A. K. The electronic properties of graphene. *Rev. Mod. Phys.* **81**, 109–162 (2009).
2. Wehling, T., Black-Schaffer, A. & Balatsky, A. Dirac materials. *Adv. Phys.* **63**, 1–76 (2014).
3. Armitage, N. P., Mele, E. J. & Vishwanath, A. Weyl and Dirac semimetals in three-dimensional solids. *Rev. Mod. Phys.* **90**, 015001 (2018).
4. Katsnelson, M. *Graphene: Carbon in Two Dimensions* (Cambridge University Press, 2012).
5. Das Sarma, S., Adam, S., Hwang, E. H. & Rossi, E. Electronic transport in two-dimensional graphene. *Rev. Mod. Phys.* **83**, 407–470 (2011).
6. Peres, N. M. R. Colloquium: The transport properties of graphene: an introduction. *Rev. Mod. Phys.* **82**, 2673–2700 (2010).
7. Hendry, E., Hale, P. J., Moger, J., Savchenko, A. K. & Mikhailov, S. A. Coherent nonlinear optical response of graphene. *Phys. Rev. Lett.* **105**, 097401 (2010).
8. Zhang, H. et al. Z-scan measurement of the nonlinear refractive index of graphene. *Opt. Lett.* **37**, 1856–1858 (2012).
9. Kumar, N. et al. Third harmonic generation in graphene and few-layer graphite films. *Phys. Rev. B* **87**, 121406(R) (2013).
10. Woodward, R. I. et al. Characterization of the second- and third-order nonlinear optical susceptibilities of monolayer MoS2using multiphoton microscopy. *2D Materials* **4**, 011006 (2016).
11. Soavi, G. et al. Broadband, electrically tunable third-harmonic generation in graphene. *Nat. Nanotechnol.* **13**, 583–588 (2018).
12. Hafez, H. A. et al. Extremely efficient terahertz high-harmonic generation in graphene by hot Dirac fermions. *Nature* **561**, 507–511 (2018).
13. Soavi, G. et al. Hot electrons modulation of third-harmonic generation in graphene. *ACS Photon.* **6**, 2841–2849 (2019).
14. Ma, Q. et al. Observation of the nonlinear hall effect under time-reversal-symmetric conditions. *Nature* **565**, 337–342 (2019).
15. Ma, J. et al. Nonlinear photoresponse of type-II Weyl semimetals. *Nat. Mater.* **18**, 476–481 (2019).
16. de Juan, F., Grushin, A. G., Morimoto, T. & Moore, J. E. Quantized circular photogalvanic effect in Weyl semimetals. *Nature Communications* **8**, 15995 (2017).
17. Rostami, H. & Polini, M. Nonlinear anomalous photocurrents in Weyl semimetals. *Phys. Rev. B* **97**, 195151 (2018).
18. Ma, J. et al. Nonlinear photoresponse of type-II Weyl semimetals. *Nat. Mater.* **18**, 476–481 (2019).
19. Cheng, B. et al. Efficient terahertz harmonic generation with coherent acceleration of electrons in the dirac semimetal cd_3as_2. *Phys. Rev. Lett.* **124**, 117402 (2020).
20. Cheng, J. L., Sipe, J. E. & Wu, S. W. Third-order optical nonlinearity of three-dimensional massless Dirac fermions. *ACS Photon.* **7**, 2515–2526 (2020).
21. Sukhachov, P. O. & Rostami, H. Acoustogalvanic effect in Dirac and Weyl semimetals. *Phys. Rev. Lett.* **124**, 126602 (2020).
22. Mikhailov, S. A. Non-linear electromagnetic response of graphene. *Europhys. Lett.* **79**, 27002 (2007).
23. Cheng, J. L., Vermeulen, N. & Sipe, J. E. Third order optical nonlinearity of graphene. *N J. Phys.* **16**, 053014 (2014).
24. Cheng, J. L., Vermeulen, N. & Sipe, J. E. Numerical study of the optical nonlinearity of doped and gapped graphene: From weak to strong field excitation. *Phys. Rev. B* **92**, 235307 (2015).
25. Cheng, J. L., Vermeulen, N. & Sipe, J. E. Third-order nonlinearity of graphene: effects of phenomenological relaxation and finite temperature. *Phys. Rev. B* **91**, 235320 (2015).
26. Mikhailov, S. A. Quantum theory of the third-order nonlinear electrodynamic effects of graphene. *Phys. Rev. B* **93**, 085403 (2016).
27. Rostami, H. & Polini, M. Theory of third-harmonic generation in graphene: a diagrammatic approach. *Phys. Rev. B* **93**, 161411(R) (2016).
28. Rostami, H., Katsnelson, M. I. & Polini, M. Theory of plasmonic effects in nonlinear optics: the case of graphene. *Phys. Rev. B* **95**, 035416 (2017).
29. Mikhailov, S. A. Theory of the strongly nonlinear electrodynamic response of graphene: a hot electron model. *Phys. Rev. B* **100**, 115416 (2019).
30. Principi, A., Bandurin, D., Rostami, H. & Polini, M. Pseudo-Euler equations from nonlinear optics: Plasmon-assisted photodetection beyond hydrodynamics. *Phys. Rev. B* **99**, 075410 (2019).
31. Hafez, H. A. et al. Terahertz nonlinear optics of graphene: from saturable absorption to high-harmonics generation. *Adv. Opt. Mater.* **8**, 1900771 (2020).
32. Rostami, H. & Juričić, V. Probing quantum criticality using nonlinear hall effect in a metallic Dirac system. *Phys. Rev. Res.* **2**, 013069 (2020).
33. Giuliani, G. & Vignale, G. *Quantum Theory of the Electron Liquid* (Cambridge University Press, Cambridge, 2005).
34. Goldman, S. P. & Drake, G. W. F. Relativistic sum rules and integral properties of the Dirac equation. *Phys. Rev. A* **25**, 2877–2881 (1982).
35. Cenni, R. On the f sum rule and its extensions. *Nuclear Phys. A* **696**, 605–622 (2001).
36. Sabio, J., Nilsson, J. & Castro Neto, A. H. *f*-sum rule and unconventional spectral weight transfer in graphene. *Phys. Rev. B* **78**, 075410 (2008).
37. Bistritzer, R. & MacDonald, A. H. Hydrodynamic theory of transport in doped graphene. *Phys. Rev. B* **80**, 085109 (2009).
38. Sun, Z., Basov, D. N. & Fogler, M. M. Third-order optical conductivity of an electron fluid. *Phys. Rev. B* **97**, 075432 (2018).
39. Sun, Z., Basov, D. N. & Fogler, M. M. Universal linear and nonlinear electrodynamics of a Dirac fluid. *Proc. Natl Acad. Sci. USA* **115**, 3285–3289 (2018).
40. Parker, D. E., Morimoto, T., Orenstein, J. & Moore, J. E. Diagrammatic approach to nonlinear optical response with application to weyl semimetals. *Phys. Rev. B* **99**, 045121 (2019).
41. Avetissian, H. K. & Mkrtchian, G. F. Impact of electron-electron coulomb interaction on the high harmonic generation process in graphene. *Phys. Rev. B* **97**, 115454 (2018).
42. Cheng, J. L., Sipe, J. E. & Guo, C. Third harmonic generation of undoped graphene in hartree-fock approximation. *Phys. Rev. B* **100**, 245433 (2019).
43. Shen, Y. *The Principles of Nonlinear Optics* (Wiley, New York, 1984).
44. Boyd, R. *Nonlinear Optics* (Academic Press, Cambridge, 2008).
45. Shon, N. H. & Ando, T. Quantum transport in two-dimensional graphite system. *J. Phys. Soc. Jpn.* **67**, 2421–2429 (1998).
46. Ando, T., Zheng, Y. & Suzuura, H. Dynamical conductivity and zero-mode anomaly in honeycomb lattices. *J. Phys. Soc. Jpn.* **71**, 1318–1324 (2002).
47. Rostami, H. & Cappelluti, E. Impurity effects and bandgap closing in massive Dirac systems. *Phys. Rev. B* **96**, 054205 (2017).
48. Aleiner, I. L. & Efetov, K. B. Effect of disorder on transport in graphene. *Phys. Rev. Lett.* **97**, 236801 (2006).
49. Castro Neto, A. H., Guinea, F., Peres, N. M. R., Novoselov, K. S. & Geim, A. K. The electronic properties of graphene. *Rev. Mod. Phys.* **81**, 109–162 (2009).
50. González, J., Guinea, F. & Vozmediano, M. A. H. Marginal-fermi-liquid behavior from two-dimensional coulomb interaction. *Phys. Rev. B* **59**, R2474–R2477 (1999).
51. Vozmediano, M. A. H. Renormalization group aspects of graphene. *Philos. Trans. R. Soc. A* **369**, 2625–2642 (2011).

52. Mishchenko, E. G. Effect of electron-electron interactions on the conductivity of clean graphene. *Phys. Rev. Lett.* **98**, 216801 (2007).
53. Leibbrandt, G. Introduction to the technique of dimensional regularization. *Rev. Mod. Phys.* **47**, 849–876 (1975).
54. Peskin, M. E. *An Introduction To Quantum Field Theory,* 1st edn. (CRC Press, 1995).
55. Baym, G. & Kadanoff, L. P. Conservation laws and correlation functions. *Phys. Rev.* **124**, 287–299 (1961).
56. Kadanoff, L. P. & Baym, G. *Quantum Statistical Mechanics,* 1st edn. (W.A. Benjamin, 1962).
57. Cappelluti, E. & Benfatto, L. Vertex renormalization in dc conductivity of doped chiral graphene. *Phys. Rev. B* **79**, 035419 (2009).
58. Dorgan, V. E., Behnam, A., Conley, H. J., Bolotin, K. I. & Pop, E. High-field electrical and thermal transport in suspended graphene. *Nano Letters* **13**, 4581–4586 (2013).
59. Berciaud, S. et al. Electron and optical phonon temperatures in electrically biased graphene. *Phys. Rev. Lett.* **104**, 227401 (2010).
60. Meric, I. et al. Current saturation in zero-bandgap, top-gated graphene field-effect transistors. *Nat. Nanotechnol.* **3**, 654–659 (2008).
61. Horng, J. et al. Drude conductivity of Dirac fermions in graphene. *Phys. Rev. B* **83**, 165113 (2011).

ACKNOWLEDGEMENTS

This work was supported by the Swedish Research Council (VR 2018-04252).

AUTHOR CONTRIBUTIONS

H.R. and E.C. conceived the overall project. H.R. performed all calculations. The manuscript was written through contributions of both authors. Both authors have given approval to the final version of the manuscript.

FUNDING

Open access funding provided by Stockholm University.

COMPETING INTERESTS

The authors declare no competing interests.

ADDITIONAL INFORMATION

Supplementary information The online version contains supplementary material available at https://doi.org/10.1038/s41699-021-00217-0.

Correspondence and requests for materials should be addressed to H.R.

Reprints and permission information is available at http://www.nature.com/reprints

Publisher's note Springer Nature remains neutral with regard to jurisdictional claims in published maps and institutional affiliations.